A Lock-and-Kill anticancer photoactivated chemotherapy agent: this article is part of a Special Issue celebrating the 50thAnniversary of the American Society for Photobiology

Geest, E.P. van; Götzfried, S. K.; Klein, D. M.; Salitra, N.; Popal, S.; Husiev, Y.; ... ; Bonnet, S.

Photochemistry and Photobiology, 20**, **: *–*

Special Issue Research Article

A Lock-and-Kill Anticancer Photoactivated Chemotherapy Agent†

Erik Pieter van Geest[1], Sina Katharina Götzfried[1], David M. Klein[1], Nadiya Salitra[1], Sorraya Popal[1], Yurii Husiev[1], Corjan J. Van der Griend[1], Xuequan Zhou[1], Maxime A. Siegler[2], Gregory F. Schneider[1] and Sylvestre Bonnet*[1]

[1]Leiden Institute of Chemistry, Leiden University, Leiden, The Netherlands
[2]Small Molecule X-ray Facility, John Hopkins University, Baltimore, MD

Received 26 July 2022, accepted 20 October 2022, DOI: 10.1111/php.13738

ABSTRACT

Photosubstitutionally active ruthenium complexes show high potential as prodrugs for the photoactivated chemotherapy (PACT) treatment of tumors. One of the problems in PACT is that the localization of the ruthenium compound is hard to trace. Here, a ruthenium PACT prodrug, [Ru(3)(biq)(STF-31)]$(PF_6)_2$ (where 3 = 3-(([2,2′:6′,2″-ter- pyridin]-4′-yloxy) propyl-4-(pyren-1-yl)butanoate) and biq = 2,2′-biquinoline), has been prepared, in which a pyrene tracker is attached *via* an ester bond. The proximity between the fluorophore and the ruthenium center leads to fluorescence quenching. Upon intracellular hydrolysis of the ester linkage, however, the fluorescence of the pyrene moiety is recovered, thus demonstrating prodrug cellular uptake. Further light irradiation of this molecule liberates by photosubstitution STF-31, a known cytotoxic nicotinamide phosphoribosyltransferase (NAMPT) inhibitor, as well as singlet oxygen *via* excitation of the free pyrene chromophore. The dark and light cytotoxicity of the prodrug, embedded in liposomes, as well as the appearance of blue emission upon uptake, were evaluated in A375 human skin melanoma cells. The cytotoxicity of the liposome-embedded prodrug was indeed increased by light irradiation. This work realizes an *in vitro* proof-of-concept of the lock-and-kill principle, which may ultimately be used to design strategies aimed at knowing where and when light irradiation should be realized *in vivo*.

INTRODUCTION

Nowadays, a plethora of transition metal complexes are considered for medicinal application against cancer, including those based on platinum, palladium, copper, or ruthenium (1). Particularly, ruthenium-based (pro)drugs have been prepared, some of which have reached clinical trials, for example NAMI-A, KP1019 and KP1339, and TLD1433 indicating that ruthenium-containing compounds are promising anticancer agents (2–5). They are particularly suitable for photodynamic therapy (PDT) and photoactivated chemotherapy (PACT), two treatment modalities where a prodrug is activated upon visible light irradiation to induce cell death only at the location of the tumor. The complex left in nonirradiated tissues remains nontoxic or much less toxic, thereby minimizing systemic toxicity for the patient (6–10). PDT typically relies on the production of reactive oxygen species (ROS) by energy or electron transfer from the excited state of the ruthenium complex to O_2. By contrast, in PACT, the excited state releases a cytotoxic compound *via* a photosubstitution reaction that is independent from the presence of O_2. This specific mode of activation of PACT is relevant for oncology, as many tumors are hypoxic ($[O_2] < 1\%$) in their core. Hypoxic tumors are more difficult to treat, not only by radiation therapy but also by PDT (11,12). The cytotoxic species in PACT may be the ruthenium polypyridyl complex itself, but the complex may also be used as a photocage to hide the anticancer activity of an organic inhibitor. In the dark, the inhibitor remains inactive as it is bound to the metal, but it is re-activated by light irradiation, which removes the ruthenium photocage (13–16). A recent example of this principle is the photoactivatable ruthenium complex [Ru(tpy)(biq)(STF-31)]Cl_2, where tpy = 2,2′:6′2″-terpyridine, biq = 2,2′-biquinoline and STF-31 = 4-((4-*t*-butyl) phenylsulfonamido)methyl-*N*-(pyridin-3-yl)benzamide (17). This PACT compound is a photocaged version of the biologically active STF-31 moiety, which is a known glucose transporter 1 (GLUT1) and nicotinamide phosphoribosyltransferase (NAMPT) inhibitor (18,19). When bound to the ruthenium metal center, STF-31 is 18 times less active than the free inhibitor. Once it is released from the metal complex, however, it regains its ability to inhibit NAMPT, leading to significant cell death (17).

For efficient application of light-activated technologies to cancer patients, it is of utmost importance that surgeons can localize the tissue that should be irradiated with light. Typically, PDT compounds (*e.g.* protoporphyrin IX) are luminescent, which is used by the surgeon not only to localize the tumor in a procedure called photodynamic diagnosis (PDD) (20–24) but also to pinpoint where to shine light *in vivo* to destroy the tumor *via* a photodynamic effect (25). Ruthenium-based PACT compounds, on the other hand, are generally not emissive. In these compounds indeed, the triplet metal-to-ligand charge transfer

*Corresponding author email: bonnet@chem.leidenuniv.nl (Sylvestre Bonnet)
†This article is part of a Special Issue celebrating the 50th Anniversary of the American Society for Photobiology.

(^{3}MLCT) excited states typically responsible for the phosphorescence of photodynamically active ruthenium compounds such as $[Ru(bpy)_3]^{2+}$ (bpy = 2,2′-bipyridine) are quenched by the low-lying triplet metal-centered (^{3}MC) excited states required for photosubstitution to take place (26). Thus, localizing the precise location where a PACT compound has been taken up, and hence where the laser should be directed to activate it, is inherently difficult.

To address this issue, we investigated in this study a new design for a ruthenium-based PACT compounds that can reveal itself after cellular uptake. The complex [Ru(**3**)(biq)(STF-31)]$(PF_6)_2$ ([**1**]$(PF_6)_2$), where **3** = 3-(([2,2′:6′,2″-terpyridin]-4′-yloxy) propyl-4-(pyren-1-yl)butanoate) bears a pyrene fluorescent tag attached to the terpyridine ligand *via* an intracellularly degradable ester linker (Fig. 1A). Before uptake, the fluorophore emission is quenched by the nearby ruthenium moiety. Upon cellular uptake, however, emission is recovered by esterase-activated cleavage of the linker, which releases free 1-pyrenebutyric acid. In fact, ester cleavage in living cells has been reported to occur quickly, which has been applied for prodrug activation, bioimaging and uptake visualization (27–30), in particular in cancer cells where esterases are overexpressed (31,32). Cancerous tissues are thus more likely to light up than noncancerous tissues. This strategy is aimed at creating an optical contrast that pinpoints the location of the PACT compound inside the tumor, to reveal where irradiation should be delivered. Upon light irradiation, the PACT compound should be able to kill the cancer cells by photo-activated release of STF-31 (Fig. 1B–D). In this work, we investigate the synthesis and properties of [**1**]$(PF_6)_2$ as a proof-of-concept of this design. The hydrophobic compound was formulated in liposomes and delivered to skin cancer cells. Our results provide the demonstration that pyrene-based fluorescence is indeed recovered *via* ester cleavage by enzymes, which can be detected *via* fluorescence microscopy, and that STF-31 release takes place, leading to phototoxicity.

RESULTS AND DISCUSSION

The synthesis of [**1**]$(PF_6)_2$ was inspired by the published protocol for making the fluorophore-free complex (17), but modified as follows (Scheme 1). First, 1,3-propanediol was reacted with 4′-Cl tpy to obtain **2**, to which the pyrene tag was attached by Steglich-esterification using 1-pyrenebutyric acid, to afford **3**. $[(Ru(\mathbf{3})Cl_2)]_2$ (compound [**4**]) was obtained *via* the metalation of ligand **3** in the presence of $[(Ru(p\text{-cymene})Cl_2)]_2$, and further converted into [Ru(**3**)(biq)(Cl)]Cl ([**5**]Cl) by coordination of the biq bidentate chelate to the ruthenium center. Thermal substitution of the chlorido ligand by the STF-31 inhibitor yielded the final compound, [**1**]$(PF_6)_2$. The reference compound [**8**]$(PF_6)_2$, which was deprived of the pyrene fluorophore, was prepared *via* the same route, but starting from ligand **2** instead of the pyrene-functionalized ligand **3**. Finally, the known complex [Ru(tpy)(biq)(STF-31)]$(PF_6)_2$ ([**9**]$(PF_6)_2$) was prepared according to the published procedure. All compounds were characterized by ^{1}H and ^{13}C NMR spectroscopy, LCMS and HRMS analysis. The purity of [**1**]$(PF_6)_2$ and [**5**]Cl was determined *via* elemental analysis (see Supporting Information).

UV–Vis experiments were employed to evaluate the thermal stability and photochemical properties of [**1**]$(PF_6)_2$. Although $[\mathbf{1}]^{2+}$ is bicationic, the strongly hydrophobic ligands and PF_6^-

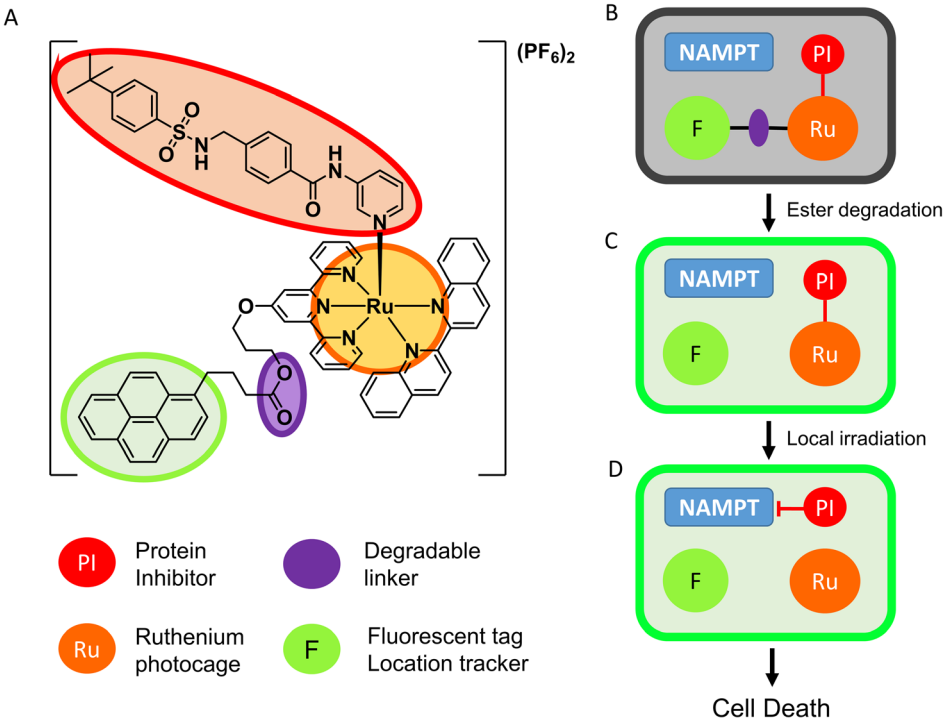

Figure 1. Design of a lock-and-kill PACT agent. (A) Molecular structure of [Ru(**3**)(biq)(STF-31)]$(PF_6)_2$ ([**1**]$(PF_6)_2$). The different functionalities are highlighted in different colors. (B–D) When the prodrug is internalized in a cell (B), the ester connection (violet) is cleaved by intracellular esterases, which makes the fluorescence of the pyrene tag (green) no longer quenched by the ruthenium complex, hence lighting up the cell (green box in C). The luminescent cells can then be treated by light irradiation, to release the STF-31 cytotoxic inhibitor (red) from the ruthenium photocage (orange, D) and induce cell death.

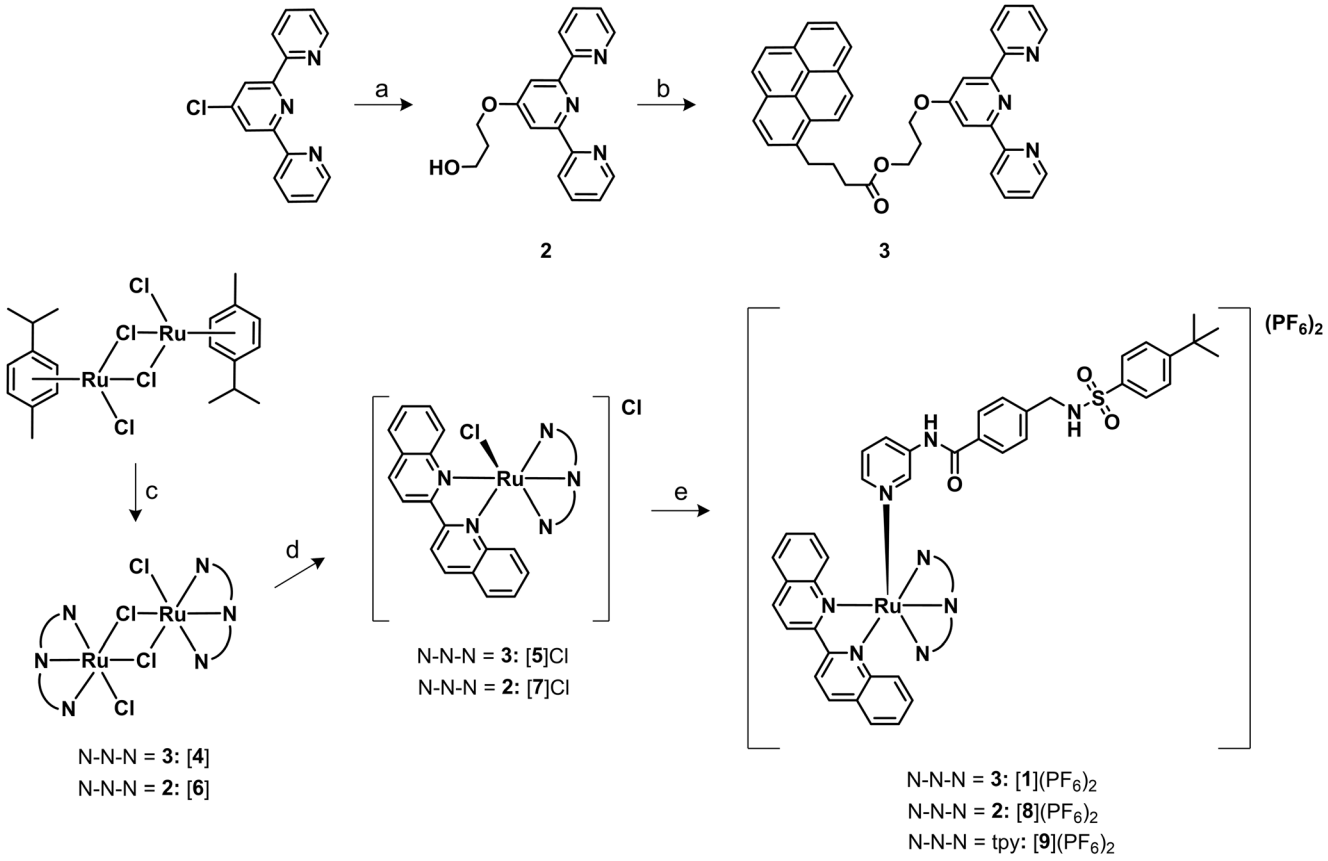

Scheme 1. Synthetic scheme toward [**1**]$(PF_6)_2$ and [**8**]$(PF_6)_2$. (a) 1,3-Propanediol, KOH, DMSO, 60°C, 5 h, 75%. (b) 1-pyrenebutyric acid, DMAP, DCC, DCM, rt, overnight, 45%. (c) Ligand 3 or 2, DCM, rt, 1 h, 68% and 92% for [**4**] and [**6**], respectively. (d) 2,2′-Biquinoline, ethylene glycol, 180°C, 2.5 h, 71% and 30% for [**5**]Cl and [**7**]Cl, respectively. (e) SFT-31 (2.0 eq.), $AgPF_6$, acetone/water 1:1, 50°C, 81% and 4% for [**1**]$(PF_6)_2$ and [**8**]$(PF_6)_2$, respectively.

counter-ions prevented complex [**1**]$(PF_6)_2$ from being soluble in water. To circumventing this problem, we dissolved [**1**]$(PF_6)_2$ ([Ru] = 25 μM) in methanol to study photosubstitution of the STF-31 ligand by methanol upon irradiation. When kept for 1 h in dark, the absorption profile did not change, reflecting that the complex was stable in such dark conditions. When the same solution was irradiated with green light (λ_{irr} = 530 nm), the absorption curve changed rapidly, corresponding to a color change from pink to purple. In a matter of minutes, the absorption maximum λ_{max} shifted from 540 nm to 554 nm, with a clear isosbestic point at 556 nm (Fig. 2A). Mass spectrometry (MS) after irradiation confirmed the full conversion of [**1**]$(PF_6)_2$ into its Ru-MeOH analogues (*m/z* = 483.6 and 966.4 for [**1** – STF-31 + MeOH]$^{2+}$ and [**1** – STF-31 + MeO]$^{+}$) and the liberated STF-31 (*m/z* = 424.2), thereby confirming the occurrence of a photosubstitution reaction.

Similar behavior was found for [**8**]$(PF_6)_2$ and [**9**]$(PF_6)_2$ in methanol upon green light irradiation (Figure S1). The photosubstitution of STF-31 was completed for all ruthenium complexes within 15 min of light exposure, that is the UV–Vis spectra showed no more change *vs*. irradiation time and MS analysis showed no remaining starting material in the irradiated solutions (Fig. 2B). The photosubstitution quantum yield (φ_{530}) was measured by calculating the slope of the amount of ruthenium-bound STF-31 complex in solution, $n_{Ru\text{-}STF}$ (in mol) *vs.* Q(t), the total amount of photons (in mol) absorbed by the reagent since the start of the reaction (*t* = 0 min). As shown in Fig. 2C, [**1**]$(PF_6)_2$ and [**8**]$(PF_6)_2$ showed almost equal photosubstitution quantum yields (φ_{530} = 0.0052 and 0.0058, respectively), which were slightly lower than that of the unmodified complex [**9**]$(PF_6)_2$ (φ_{530} = 0.012 in the same conditions). This latter value was similar to the φ_{625} = 0.013 value reported in water for the same complex using red light (625 nm, see reference (17)), showing that photosubstitution was as efficient in water as in methanol, and also mostly independent from the irradiation wavelength. According to these results, the φ_{530} value was significantly affected by the ether moiety in the 4′ position of the tpy ligand. We hypothesize that the electron-donating effect of the ether group in [**1**]$(PF_6)_2$ and [**8**]$(PF_6)_2$ is responsible for these changes: this electron-donating group increases the electron density of the tpy ligand, hence the ligand field splitting energy of the complex, and hence the energy gap between the ^{3}MLCT and the ^{3}MC state. As a result, photosubstitution is slower compared to other processes taking place from the ^{3}MLCT, which lowers the photosubstitution quantum yield φ_{530}. On the other hand, the presence of the pyrene moiety on the ether-modified tpy ligand of [**1**]$(PF_6)_2$ did not impair the photoreactivity of the ruthenium complex, which was identical to that of [**8**]$(PF_6)_2$, probably because of the high energy of the pyrene-centered excited states, compared to the ruthenium-involving ^{3}MLCT and ^{3}MC states. When irradiation of [**1**]$(PF_6)_2$ and [**9**]$(PF_6)_2$ was performed in the region where pyrene absorbs (λ_{irr} = 365 nm, Figure S2), the

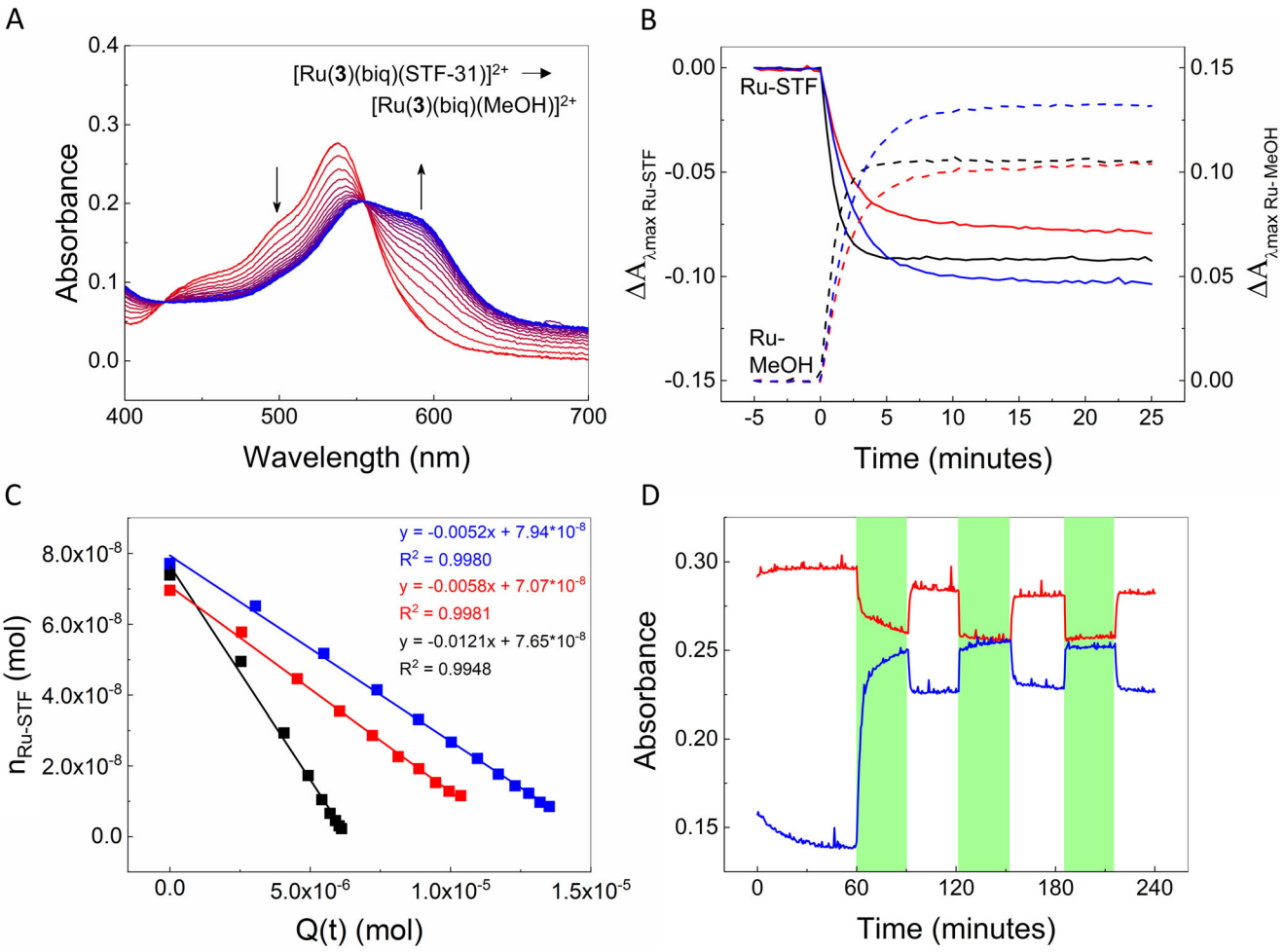

Figure 2. Photosubstitution of STF-31. (A) Evolution of absorbance of a solution of $[\mathbf{1}](PF_6)_2$ (25 μM) in pure methanol, upon irradiation with green light (λ_{irr} = 530 nm, photon flux = 1.36 × 10^{-7} mol·s^{-1}) after 1 h equilibration in the dark at rt. Spectra display the absorbance at the start of irradiation (red) to 10 min after irradiation started (blue), recorded every 30 s. (B) Absorbance change (ΔA at λ_{max}) *vs.* irradiation time for $[\mathbf{1}](PF_6)_2$, $[\mathbf{8}](PF_6)_2$ and $[\mathbf{9}](PF_6)_2$ (denominated Ru-STF: blue, red and black solid line, resp. 540, 538 and 531 nm), and for their corresponding photoproducts (denominated Ru-MeOH: blue, red and black dashed line, resp. 554, 552 and 580 nm). (C) Evolution of the amount of Ru-STF complexes in solution, $n_{Ru\text{-}STF}$ in mol, *vs.* $Q(t)$ (in mol), defined as the total amount of photons absorbed by the Ru-STF complexes since t = 0 min, for $[\mathbf{1}](PF_6)_2$ (blue), $[\mathbf{8}](PF_6)_2$ (red) and $[\mathbf{9}](PF_6)_2$ (black); the slope of these plots are the quantum yields φ_{530} of the photosubstitution reaction in pure methanol. (D) Absorbance *vs.* time at λ_{max} for $[\mathbf{1}](PF_6)_2$ and the photoproduct (red: λ_{max} = 540 nm and blue: λ_{max} = 587 nm) in a methanol/water = 95:5 (v/v) mixture. Irradiation started at t = 60 min and was switched off and on (green bars) repeatedly, every 30 min. Spectra were recorded every 30 s.

photosubstitution kinetics observed at this wavelength were similar to those obtained for green light irradiation, that is in such conditions the reaction was finished within a few minutes. In addition, no significant increase of the rate of photosubstitution was found for $[\mathbf{1}]^{2+}$, compared to $[\mathbf{9}]^{2+}$, suggesting that FRET did not play a significant role when $[\mathbf{1}]^{2+}$ was irradiated at 365 nm. Overall, photosubstitution of STF-31 in $[\mathbf{1}]^{2+}$ was affected by the presence of the ether linker on the terpyridine ligand, but not by the presence of the covalently bound pyrene moiety.

For all three complexes, STF-31 photosubstitution in methanol was an irreversible process, that is in the dark no back-coordination of STF-31 to the ruthenium methanol complex was observed. Interestingly, in presence of 5% water (MeOH/H_2O = 95:5 (v/v)), the photoreaction seemed to become reversible. After reaching the steady state, switching off the light source led to reverse changes of the absorption spectrum of the solution, compared with the changes observed under light irradiation, and identical isosbestic points. In addition, switching on and off the light source twice more led to identical time evolution of the absorbance spectra (Fig. 2D, Figure S3A,B), and the spectra at the steady state (under light irradiation) or thermal equilibrium (in the dark) were identical (Figure S3C, D). Based on these data, we hypothesize that the photosubstitution reaction was reversible in such conditions, that is that STF-31 may partly bind back to ruthenium in the dark. Such reversibility solely obtained upon adding water may be attributed to solvation effects: in pure methanol, both the liberated STF-31 and the ruthenium photoproduct are soluble enough to diffuse away from each other, which prevents them from reacting back thermally to form $[\mathbf{1}]^{2+}$. In the presence of water, however, the reaction products diffuse less than in methanol due the high lipophilicity of the compound. This effect keeps both photoproducts close to each other by the water molecules in a solvent "cage," and the back-reaction is thus more likely to occur (33). Such reversibility, although interesting, is

probably not relevant to explain what happens in a biological setting: cells are full of hydrophobic regions (proteins, membranes, DNA, *etc.*), which would be capable of solvating the photoproducts of photosubstitution in $[\mathbf{1}]^{2+}$, thereby preventing back-coordination. Overall, all three complexes uncaged the STF-31 ligand upon green light irradiation and adding the pyrene group did not prevent this photosubstitution to occur.

As the pyrene moiety and the ruthenium complex can be addressed independently by shining UV or visible light, respectively, it was also possible to study the effect of the ruthenium complex on the emission of the fluorophore. We postulated that the presence of the ester linker is crucial for altering the emission properties of the pyrene group, and that such quenching by the ruthenium complex is relieved once the ester linker is cleaved (Fig. 3A). In order to verify this hypothesis, we studied the luminescence properties of the intact complexes $[\mathbf{1}](PF_6)_2$ and [**5**]Cl and that of the ester degradation products [**7**]Cl and 1-pyrenebutyric acid in methanol. Complex $[\mathbf{1}](PF_6)_2$ (50 μM) was found to be nonfluorescent, while complex [**5**]Cl showed a weak emission at λ_{em} = 395 and 375 nm upon excitation at λ_{ex} = 354 nm. In comparison, upon mixing 1-pyrenebutyric acid and [**7**]Cl at the same concentration, a strong emission was recorded at λ_{em} = 395 and 375 nm, indicating that diffusional quenching by an unbound ruthenium complex was not efficient (Fig. 3B and Figure S4). Nevertheless, it did occur to some extent, as 1-pyrene butyric acid alone exhibited stronger fluorescence at λ_{em} = 375–400 nm in the absence of a ruthenium complex. The ruthenium complex absorbed in the region where free 1-pyrenebutyric acid emitted, so a filter effect is also likely here (Fig. 3C). Most importantly, fluorescence quenching was much stronger when the pyrene group was covalently attached to the complex. We hypothesized quenching occurred *via* Förster resonance energy transfer (FRET), as reported for a pyrene-labeled, photosubstitution-inactive ruthenium(II) trisbipyridine complex (34). The Förster distance R_0 at which quenching of the fluorescence by FRET has an efficiency of 50% was calculated to be 24 Å (see Supporting Information). In a model of $[\mathbf{1}]^{2+}$ (simulated with Yasara), we evaluated the Ru-pyrene distance to be ~20 Å (Figure S5), which is quite smaller than R_0. This short distance is compatible with an efficient quenching of the pyrene tag by FRET to ruthenium in compounds $[\mathbf{1}]^{2+}$, and the corresponding FRET efficiency was calculated to be φ_{FRET} = 0.76.

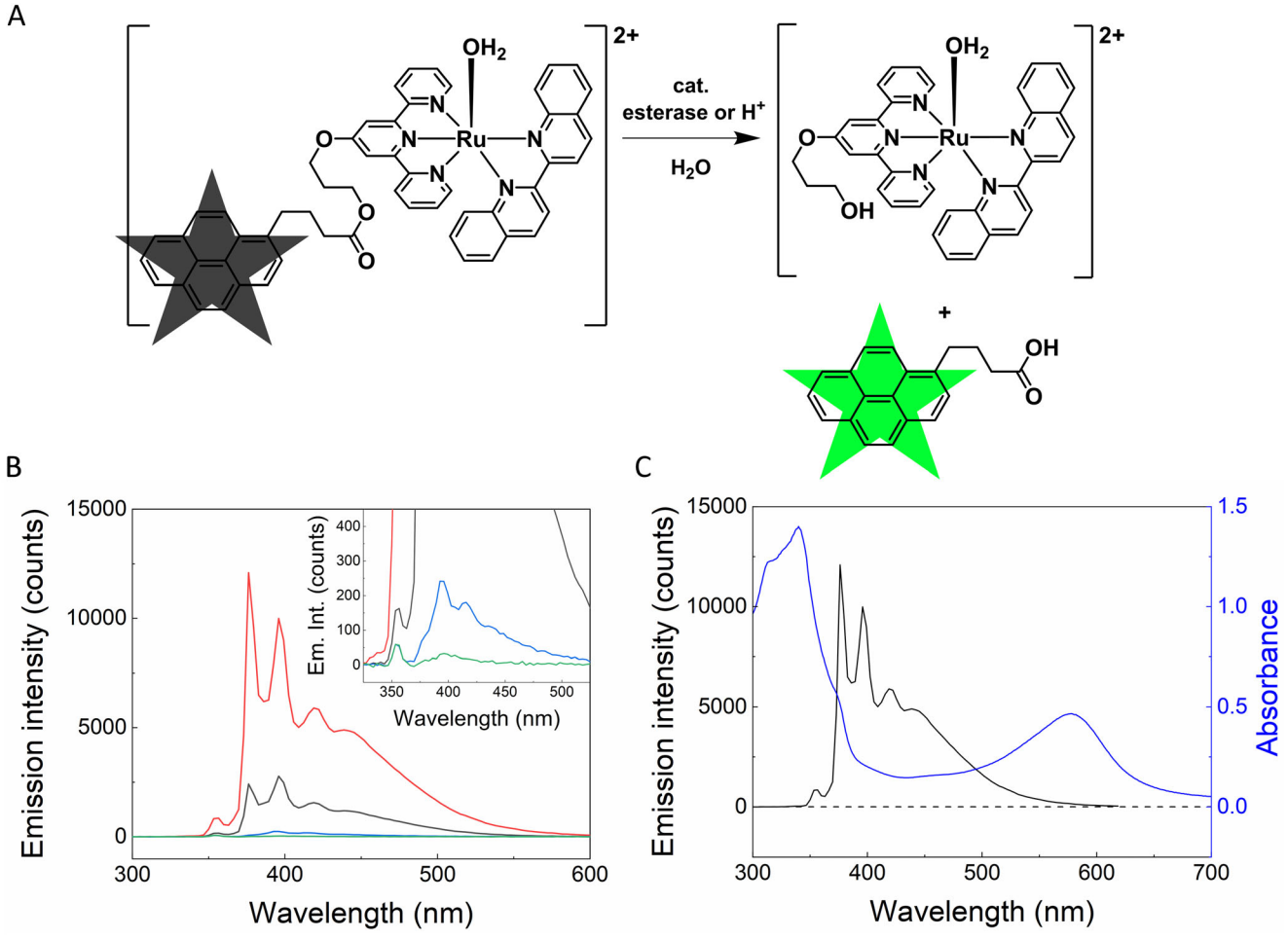

Figure 3. Quenching of the pyrene tag emission by ruthenium, and effect of ester degradation on 1-pyrenebutyric acid emission. (A) Upon cleavage of the ester bond, the 1-pyrenebutyric acid (black star) is liberated, and is no longer quenched by the ruthenium complex and shows strong fluorescence (green star). (B) Emission intensity of a methanol solution of $[\mathbf{1}](PF_6)_2$ (green), [**5**]Cl (blue), a 1:1 mixture of [**7**]Cl and 1-pyrenebutyric acid (black), and 1-pyrenebutyric acid alone (red), λ_{ex} = 354 nm. Concentration of all species was 50 μM. Inset: zoom of emission intensity (Em. Int.). (C) Spectral overlap between the emission of 1-pyrenebutyric acid (black, left axis, λ_{ex} = 354 nm) and absorbance of [**7**]Cl (blue, right axis), both 50 μM in methanol. Dashed line is the baseline.

Water solubility is of utmost importance for a compound to be tested for biological purposes. As previous tests highlighted a very poor water solubility for this family of compounds, liposomes were chosen as drug carriers to bring these molecules into cancer cells (35). Complexes [**1**]$(PF_6)_2$ and [**5**]Cl (as a reference) were hence embedded into DSPC/NaDSPG/Cholesterol 53:21:26 liposomes prepared in Dulbecco's phosphate buffer (PBS), a formulation called AmBisome® (where DSPC = distearoylphosphatidylcholine and NaDSPG = 1,2-distearoyl-sn-glycero-3-phospho-rac-glycerol, sodium salt (36)). The theoretical concentration of ruthenium in the liposome formulation was 1 mol%, but inductively-coupled plasma mass spectrometry (ICP-MS) was used to experimentally establish the real ruthenium concentration in the liposomes, as lipophilic compounds are sometimes retained in the extrusion filters used during liposome preparation. An average bulk ruthenium concentration of 42 μM ([**1**]$(PF_6)_2$) and 48 μM ([**5**]Cl) was found (Table S1), instead of the calculated 100 μM, confirming that some ruthenium was indeed lost during extrusion. Size distribution analysis by dynamic light scattering (DLS) showed that liposomes loaded with [**1**]$(PF_6)_2$ or [**5**]Cl possessed an average diameter of 353 nm or 307 nm and a polydispersity index (PDI) of 0.25 or 0.14, respectively (Table S1). These characteristics remained stable when the liposomes were kept in the dark over 15 days at room temperature (Table S2). Last but not least, the UV–Vis spectral evolution of a liposome solution loaded with [**1**]$(PF_6)_2$ displayed two distinct isosbestic points at 570 and 628 nm upon irradiation with green light (λ_{irr} = 528 nm, 7.00 mW, Figure S6), pointing to a selective and unique photoreaction, similar as what was observed in homogeneous methanol solutions. Complex [**1**]$(PF_6)_2$ is thus still light-activatable when embedded in a liposome, as demonstrated earlier (37).

In the next step, we designed an esterase assay aiming at investigating whether the ester linker between the ruthenium moiety and the pyrene fragment was indeed degradable by esterases, and how such a cleavage would influence the fluorescence of the pyrene dye. Therefore, a solution of porcine liver esterase (PLE, 1 U mL^{-1}) in PBS was mixed with liposomes (as previously prepared) containing either [**1**]$(PF_6)_2$ or [**5**]Cl (10 μM). The fluorescence of the solution was recorded *vs.* time (λ_{ex} = 320 nm). Upon addition of the PLE solution, fluorescence started to build up for both types of liposomes, as depicted in Fig. 4A,B. Here, the fluorescence intensity is displayed at λ_{em} = 386 nm, which is also the emission maximum for free 1-pyrenebutyric acid. When PLE was not added, no increase in fluorescence was observed (control). These results demonstrated that the ester linker was indeed cleaved by enzymatic activity for both complexes, although the metal complex was embedded in the lipid membrane environment. As a note, the sensitivity of the ester linker to acids was also demonstrated, at least for [**5**]Cl: when trying to crystalize this complex in presence of triflic acid, an aqua complex with a broken ester linkage was obtained (Figure S7). Overall, in a controlled chemical environment the lead compound [**1**]$(PF_6)_2$ can hence release two fragments: the GLUT1/NAMPT inhibitor upon irradiation with visible light, and the pyrene moiety in the presence of esterases (or acid). Upon cleavage of the ester linker the pyrene group can be detected by its fluorescence, since it is no longer quenched by the covalently bound ruthenium complex.

With these results in hands, we conducted *in vitro* studies on the cellular uptake of the ruthenium-functionalized liposomes in A375 human skin melanoma cells and followed their fluorescence intensity using fluorescence microscopy. For uptake, the pyrene label was used as a probe. Liposomes with a calculated 1 mol% of 1-pyrenebutyric acid loading served as a positive control. After 24 h incubation in the dark, cells treated with such liposomes were indeed efficiently stained by pyrene, albeit only at relatively high treatment concentrations (>5 μM), while control cells and cells treated with pyrene-free liposomes did not show emission at all (Figure S8). On the other hand, upon treatment with [**5**]Cl only the cells treated with the highest concentration (20 μM) were found to be stained by pyrene. Unfortunately, at such concentrations most cells perished (Fig. 4C). For liposomes loaded with [**1**]$(PF_6)_2$, however, no fluorescence was observed even after 24 or 72 h incubation. These data are in accordance with those obtained using PLE (Fig. 4A), in which [**5**]Cl showed a faster release of the pyrene moiety. Also, when the liposome-containing medium was refreshed with liposome-free medium after 24 h incubation to avoid cell death, no blue emission was detected. Even the control liposomes loaded with 1-pyrenebutyric acid did not show any fluorescence 24 h after exchanging the medium, which shows that such conditions are not optimal for such an experiment. This observation suggests that the pyrene moiety may be metabolized by the cells, or pumped out, within 24 h. It may also be that the ester linker between the pyrene fluorophore and the ruthenium prodrug is not efficiently metabolized by esterases in the lysosomes, and hence that the pyrene tag buildup in cells is too low to be detected. Nevertheless, we have demonstrated that cells can indeed be stained by pyrene, revealing the presence of the ruthenium prodrug, but our study also highlights the fact that the cells may die before they are stained, if the prodrug (or here, the liposomes) are too toxic. Thus, the success of the strategy investigated in this work appears to rely on the delicate balance between drug toxicity and efficiency of the fluorescent tag cleavage.

The influence of the Ambisome® liposomes loaded with 1 mol% [**1**]$(PF_6)_2$ or [**5**]Cl on cell viability was evaluated on A375 cells *via* a colorimetric Sulforhodamine B (SRB) assay, following a published protocol (38). The cells were seeded at t = 0 min, treated at 24 h and either activated by green light irradiation at 48 h (λ_{irr} = 520 nm, power density 14.6 mW cm^{-2}, light dose = 26.3 J cm^{-2}), or kept in the dark. Further incubation for 48 h was terminated by the SRB end-point cell viability assay (t = 96 h). Label-free liposomes and liposomes loaded with 1% 1-pyrenebutyric acid served as vehicle controls. The highest concentrations of the two ruthenium compounds were chosen as low as possible (25 μM) as these compounds absorb at the same wavelength as the SRB dye used to quantify cell viability in the endpoint assay. In the dark, the drug-free liposomes displayed no cytotoxic effects in the chosen cell line up to a lipid bulk concentration of 10 mM (Figure S9A), but after exposure to green light a slightly reduced cell proliferation was observed. Liposomes loaded with 1% 1-pyrenebutyric acid illustrated an anti-proliferative effect at high pyrene concentration only ($EC_{50,dark}$ = 32.9 μM, $EC_{50,light}$ = 16.1 μM), with small differences between dark and light conditions that corresponded to a photoindex (PI = $EC_{50,dark}/EC_{50,light}$) of 2.0 (Figure S9B). Similar light-induced effects were observed for [**5**]Cl (Fig. 5A). In the dark, an $EC_{50,dark}$ value of 3.63 μM was observed while after irradiation cell survival was inhibited at an $EC_{50,light}$ = 1.87 μM (PI = 1.94). As expected, complex [**1**]$(PF_6)_2$, displayed high cytotoxicity ($EC_{50,dark}$ = 1.93 μM; $EC_{50,light}$ = 0.26 μM) and a

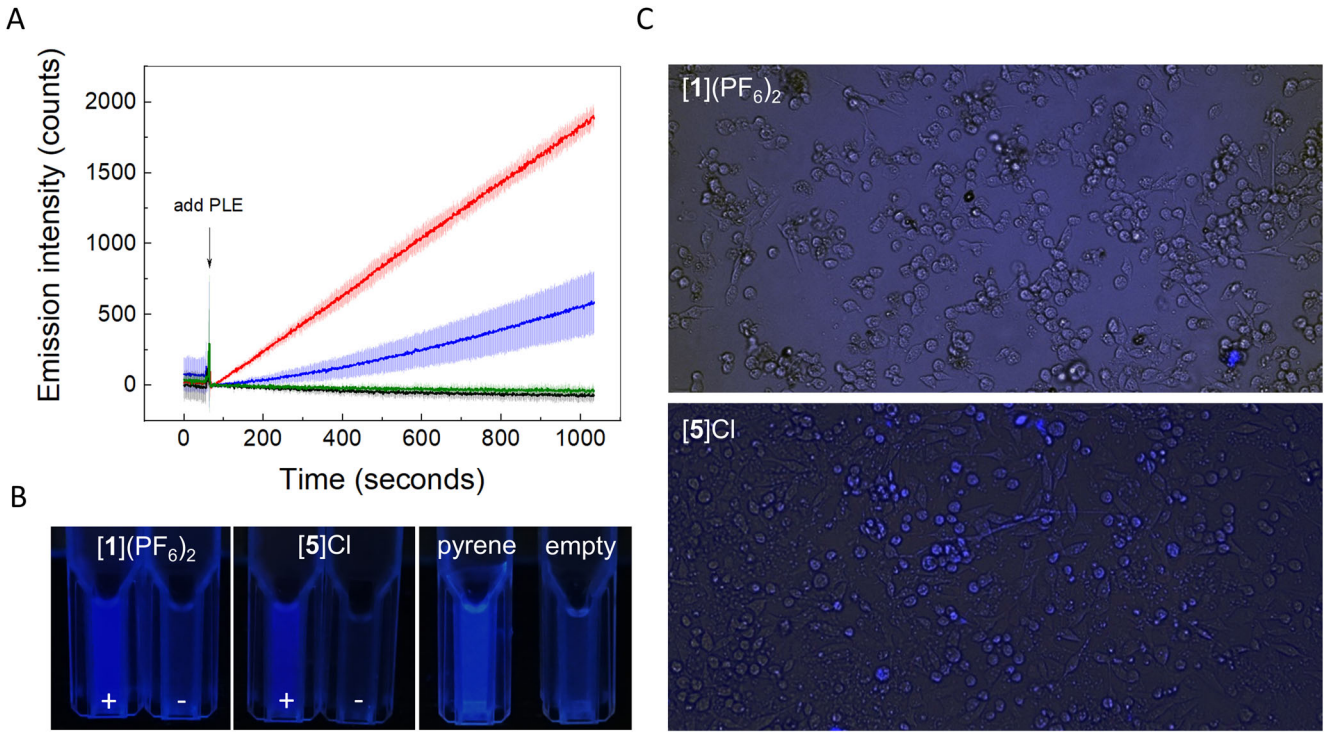

Figure 4. Fluorescence activation. (A) Pyrene emission intensity *vs*. incubation time for Ambisome® liposomes ([lipid] = 1 mM) bearing a calculated loading of 1 mol% Ru in PBS (λ_{ex} = 320 nm, λ_{em} = 386 nm). After a short stabilization period, a solution of the enzyme porcine liver esterase (PLE, final concentration 1 U mL^{-1}) in PBS was added (indicated by the arrow). For the reference samples, the PLE solution was replaced by PBS. Blue/black and red/green: [**1**]$(PF_6)_2$ and [**5**]Cl with/without PLE, respectively. For comparison, the emission intensity value is set to 0 right after PLE addition. Statistical errors are indicated by the shaded area in the corresponding color. (B) Color-enhanced photograph of liposome solutions with calculated 1 mol% loading of [**1**]$(PF_6)_2$, [**5**]Cl, 1-pyrenebutyric acid, and without loading, after 7 days storage at rt, with or without PLE incubation, indicated with + or −. (C) Fluorescence microscopy images of A375 cells treated for 24 h in the dark with Ambisome® liposomes containing [**1**]$(PF_6)_2$ or [**5**]Cl (calculated [Ru] = 20 μM in PBS) in DAPI modus.

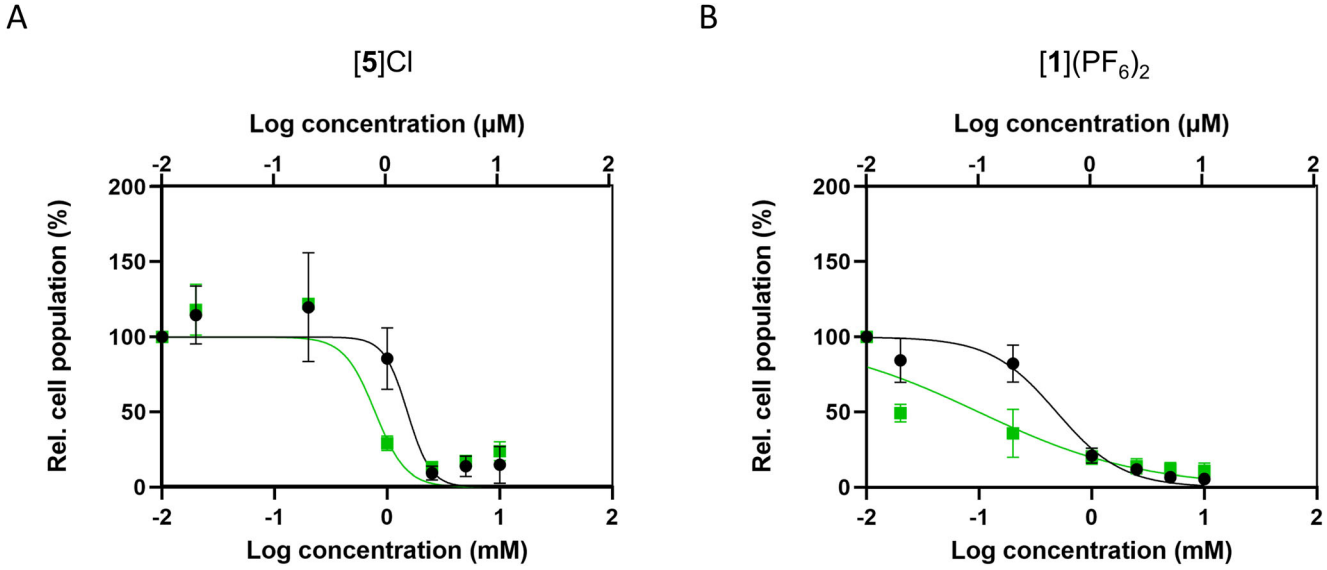

Figure 5. Cellular toxicity of Ambisome® liposome functionalized with 1 mol% of [**1**]$(PF_6)_2$ or [**5**]Cl under greenlight irradiation and in the dark. The dose response curves show the endpoint (t = 96 h) relative cell viability according to the SRB assay for A375 cells treated with AmBisome® liposomes loaded with (A) [**5**]Cl or (B) [**1**]$(PF_6)_2$. The X-axes shows the calculated ruthenium concentration (top) and the lipid concentration (bottom).

comparatively high PI value of 7.50, thus showing a higher light-activation efficiency than [**5**]Cl (Fig. 5B). Though for [**1**]$(PF_6)_2$ a PACT mechanism driven by light-induced delivery of STF-31 is very likely, for [**5**]Cl the cause of the phototoxic effect was less obvious. To investigate any photodynamic effect, singlet oxygen ($^1O_2$) production was quantified by measuring the

emission peak of $^1O_2$ at 1270 nm upon irradiation of the complex with blue light in CD_3OD (λ_{irr} = 450 nm) (39). Compound $[Ru(bpy)_3]Cl_2$, a well-known producer of $^1O_2$, served as reference (φ_Δ = 0.73) (40,41). For [**5**]Cl a $^1O_2$ generation quantum yield φ_Δ of only 0.0042 was found (Figure S11 and Table S4). This complex is thus a very weak producer of $^1O_2$. Yet, for the free 1-pyrenebutyric acid, we found that φ_Δ = 0.078 (Figure S12 and Table S5), meaning that this species is active as a PDT agent after it is cleaved from the ruthenium complex. Thus, next to PACT and PDD, PDT also occurs here, making of [**1**]$(PF_6)_2$, in fact, a triple-action prodrug. It should be noted that the mode-of-action of this prodrug is wavelength-dependent: PDT and PACT can be activated simultaneously using UV or blue light, where free pyrene absorbs light significantly (Figure S5), while PACT will be the main mode of action to be activated when irradiation is performed with green light, that is at wavelengths where pyrene poorly absorbs.

To correlate the cytotoxicity results to the actual concentration of ruthenium in the cells, cellular uptake quantification studies were done using ICP-MS. After 24 h incubation the intracellular accumulation of liposome loaded with 1 mol% of [**5**]Cl was 2.25 times higher (26.1 ± 0.5 ng million cells^{-1}) than that of liposomes loaded with 1 mol% of [**1**]$(PF_6)_2$ (11.6 ± 2.7 ng million cells^{-1}). Even though the uptake of [**1**]$(PF_6)_2$ was lower than that of uncaged [**5**]Cl (in the same conditions), liposomes loaded with [**1**]$(PF_6)_2$ showed a higher PI value, which can probably be attributed to the light-induced release of the cytotoxic STF-31 ligand. From the cytotoxicity and uptake results, we conclude that the light-induced toxicity of liposome-embedded complex [**1**]$(PF_6)_2$ resulted in a lower EC_{50} value, likely not only due to the release of the toxic STF-31 ligand upon light irradiation, but also due to a contribution of the ruthenium-based photoproduct remaining after release of STF-31.

CONCLUSIONS AND OUTLOOK

The ruthenium complex [**1**]$(PF_6)_2$ bearing a hydrolysable fluorophore and a light-cleavable STF-31 ligand was synthesized as a proof-of-concept that a fluorescent tag can be quenched when covalently attached to ruthenium, and become visible upon entering into a cancer cell. Importantly, the presence of the pyrene moiety did not modify the photosubstitution reactivity of the ruthenium-based PACT complex, while the presence of the ruthenium complex did strongly quench the emission of the fluorophore. As a consequence of the different fragments used in the design of [**1**]$(PF_6)_2$ it ended up being highly hydrophobic, which required liposomes for delivering this molecule into A375 skin cancer cells. Even after embedding in the liposome membrane, the ester bond in [**1**]$(PF_6)_2$ could be cleaved by esterases in the aqueous phase, which "unlocked" the fluorescence of the pyrene tag. At the same time, such cleavage also unlocked the ability of the pyrene moiety to generate singlet oxygen, and hence to generate a photodynamic effect on top of its PACT mode of action. Enzymatic ester cleavage was significantly faster for complex [**5**]Cl, an analogue of [**1**]$(PF_6)_2$ deprived of the STF-31 inhibitor, than for [**1**]$(PF_6)_2$, showing the influence of the molecular formula of the ruthenium compound on its position in the membrane and availability to enzymatic cleavage. The cytotoxicity of Ambisome® liposomes loaded with 1 mol% of [**1**]$(PF_6)_2$ increased significantly upon green light irradiation (PI = 7.50), as expected for a PACT compound. Most importantly, we were able to detect by fluorescence microscopy traces of the released pyrene fluorophore in A375 skin cancer cells treated for 24 h with liposomes loaded with [**5**]Cl. Cleavage of the ester bond thus occurred *in cellulo*, which validates our approach. Yet, in the same conditions, this effect was not observed for liposomes loaded with [**1**]$(PF_6)_2$. This contradicting result appears to be a consequence on the one hand of their lower cellular uptake and slower enzymatic ester cleavage, compared with liposomes loaded with [**5**]Cl, which renders detection by fluorescence microscopy more difficult; and on the other hand by their higher cytotoxicity, which imposes to work at low concentrations if one tries to observe the fluorescence of the pyrene tag in living cells.

This study highlights the intricate relationship between the dark toxicity and photoactivation efficiency of the PACT compound, its hydrophobicity, its reactivity to enzymatic cleavage of the dye, and its cellular uptake and localization, all the more when supported in a liposome drug delivery system like the one presented in this work. In order to build a practical system working *in vivo*, these parameters will need to be optimized altogether. We envision that the principles of fluorescence activation by prodrug metabolism prior to light activation may be used in the future for visualizing PACT prodrug uptake in tumors *in vivo*. If prodrug metabolism in cancer cells is faster, the tumor may indeed light up and show contrast with healthy tissues in the operating room, thus showing a surgeon where to shine light. Moreover, the ability to perform both PDT and PACT opens up multiple routes towards cell death, which will decrease the likeliness of the tumor cells to develop drug resistance. In conclusion, the ruthenium prodrug we have reported here is a truly multi-action phototherapeutic agent, as it covers three different phototherapies (PDD, PDT and PACT) at once in one compound, accessed through multiple activation strategies. The strategy of multifunctional prodrugs presented here can pave the way to designing more versatile (photo)activatable prodrugs that help to trace the fate of the drug *in vivo*, while at the same time reducing drug resistance *via* the opening of multiple cell killing routes.

Acknowledgements—NWO is kindly acknowledged for a VICI grant to SB. The authors kindly acknowledge Winant van Os for scientific discussions and support with the preparation of the liposomes, and Dr. Vadde Ramu for synthesis of the previously reported complex [**9**]$(PF_6)_2$. This work was supported by the European Research Council under the European Union's Seventh Framework Programme (FP/2007-2013)/ERC Grant Agreement no. 335879 project acronym "Biographene" and the Netherlands Organization for Scientific Research (NWO-VIDI 723.013.007).

CONFLICT OF INTEREST

There is no conflict of interest to declare.

SUPPORTING INFORMATION

Additional supporting information may be found online in the Supporting Information section at the end of the article:

Figure S1. Evolution of the absorption spectrum of a solution of [**8**]$(PF_6)_2$ and [**9**]$(PF_6)_2$ (respectively A and B, 25 μM) in methanol upon irradiation with green light (λ_{irr} = 530 nm, photon flux = 1.36×10^{-7} mol·s^{-1}). Spectra shown between

t = 0 min (red spectrum) and t = 10 min (blue spectrum). Spectra were recorded under air, every 30 s. Temperature: 298 K.

Figure S2. Evolution of the absorption spectrum of a solution of [**1**]$(PF_6)_2$ and [**9**]$(PF_6)_2$ (respectively A and B, 50 μM, $A_{365} \sim 0.4$ for both compounds) in methanol upon irradiation with UV light (λ_{irr} = 365 nm, 23.8 mW). Spectra shown between t = 0 min (red spectrum) and t = 30 min (blue spectrum). Spectra were recorded under air, every 30 s. Temperature: 298 K. (C) Absorbance change ($\Delta A_{530\ nm}$) *vs*. irradiation time for [1]$(PF_6)_2$ and [**9**]$(PF_6)_2$ under UV light irradiation (blue and black solid line, respectively), and for their corresponding photoproducts (Ru-MeOH: blue, black dashed line, at respectively 585 and 590 nm).

Figure S3. Evolution of the UV–vis spectrum for a solution of [**1**]$(PF_6)_2$ (25 μM) in methanol/water (95:5) upon 1st (A) and 2nd (B) irradiation with green light (λ_{irr} = 530 nm, photon flux = 1.36×10^{-7} mol·s^{-1}). Spectra shown between t = 0 min (red spectrum) and t = 10 min (blue spectrum). Spectra were recorded under air, every 30 s. Temperature: 298 K. (C) Absorption spectra at the end of three dark and three light irradiation periods. From black to light gray: dark reaction, 1st, 2nd and 3rd thermal coordination. From dark red to orange: 1st, 2nd and 3rd light irradiation period. (D) Time evolution of the color-coded absorption spectra of the solution shown in A–C showing the reversibility of the spectral signature of the reaction during light (on)/dark (off) switching of the light source.

Figure S4. 2D Luminescence plots of [**1**]$(PF_6)_2$, [**5**]Cl, [**7**]Cl, [**7**]Cl + 1-pyrenebutyric acid and 1-pyrenebutyric acid (respectively A–E, 50 μM) in methanol. Compounds are schematically represented by the components of the intact complex as orange, green and blue boxes. Excitation (EX) wavelength (λ_{ex}) is plotted on the x-axis and emission (EM) wavelength (λ_{em}) on the y-axis. Rainbow color scale shows relative fluorescence intensity, with red for high emission and blue for no emission. Scale multiplier is indicated by the number in the bottom right of each panel. Detections at $\lambda_{ex} = \lambda_{em}$ are due to scattering of the excitation laser by the solutions.

Figure S5. (A) Spectral overlap ($F_D(\lambda)\varepsilon_A(\lambda)\lambda^4$) of the emission intensity, total area normalized to 1, ($F_D(\lambda)$) of the donor 1-pyrenebutyric acid, and the extinction coefficient of the acceptor [**8**]Cl ε_A, multiplied by λ^4, *vs*. the wavelength (λ). (B) Yasara simulation of $[\mathbf{1}]^{2+}$, the Ru-pyrene distance r (from the ruthenium ion to the center carbon atoms of the pyrene moiety) is indicated by the dashed lines; r was found to be 20.2 Å.

Figure S6. Evolution of absorbance of a solution of complex [**1**]$(PF_6)_2$ (25 μM, calculated 1% loading) loaded on AmBisome® liposomes (DSPC/NaDSPG/Cholesterol 53:21:26, lipid concentration = 2.5 mM) in Dulbecco's phosphate buffer upon green light irradiation (λ = 528 nm, P = 7.00 mW) at 37°C.

Figure S7. Displacement ellipsoid plot (50% probability) of [Ru(**2**)(biq)(OH_2)]$(OTf)_2$ crystals, obtained from a solution of [**5**]Cl in a methanol that was acidified with TFA. Hydrogen atoms and the triflate counterions have been omitted for clarity.

Figure S8. Fluorescence microscopy images of A345 skin cancer cells. Top: control cells that are untreated. Middle: A345 cells that are treated with "empty" liposomes, *that is*, liposomes that were not loaded with an additional molecule other than lipids or cholesterol. Bottom: cells treated with liposomes loaded with 1-pyrenebutyric acid, calculated loading 1% = 20 μM. Images produced in DAPI mode.

Figure S9. SRB assay dose response curves for A375 skin cancer cells treated with (A) empty AmBisome® liposomes, or (B) with AmBisome® liposomes with a loading of 1-pyrenebutyric acid (1% calculated loading).

Figure S10. Singlet oxygen ($^1O_2$) production for [**5**]Cl. The presence of $^1O_2$ is shown by emission peak at 1270 nm. Emission spectra are shown for solutions of complex [**5**]Cl and reference compound $[Ru(bpy)_3]Cl_2$ (both 25 μM in MeOD) in blue and black, respectively. The emission integrated area E between 1200 and 1350 nm that were used for the quantum yield calculations are displayed under the curves.

Figure S11. $^1O_2$ phosphorescence in CD_3OD (normalized data).

Table S1. Average diameter (Zave) and polydispersity index (PDI) as determined by DLS and total ruthenium concentration determined by ICP-MS of Ambisome® liposomes (DSPC/NaDSPG/Cholesterol 53:21:26, lipid concentration = 10 mM) with a calculated loading of 1% of complex [**1**]$(PF_6)_2$ or [**5**]Cl.

Table S2. Ruthenium-loaded liposome stability over days, studied with DLS.

Table S3. Selected bond length (Å) and torsion angle (°) for [Ru(**2**)(biq)(OH_2)]$(OTf)_2$.

Table S4. Determination of singlet oxygen quantum yields.

Table S5. Determination of singlet oxygen quantum yields (II).

Section S1. Materials and Methods.

REFERENCES

1. Mjos, K. D. and C. Orvig (2014) Metallodrugs in medicinal inorganic chemistry. *Chem. Rev.* **114**, 4540–4563.
2. Clarke, M. J. (2002) Ruthenium metallopharmaceuticals. *Coord. Chem. Rev.* **232**, 69–93.
3. Morris, R. E., R. E. Aird, P. D. Murdoch, H. M. Chen, J. Cummings, N. D. Hughes, S. Parsons, A. Parkin, G. Boyd, D. I. Jodrell and P. J. Sadler (2001) Inhibition of cancer cell growth by ruthenium(II) arene complexes. *J. Med. Chem.* **44**, 3616–3621.
4. Sava, G., S. Zorzet, C. Turrin, F. Vita, M. Soranzo, G. Zabucchi, M. Cocchietto, A. Bergamo, S. DiGiovine, G. Pezzoni, L. Sartor and S. Garbisa (2003) Dual action of NAMI-A in inhibition of solid tumor metastasis: Selective targeting of metastatic cells and binding to collagen. *Clin. Cancer Res.* **9**, 1898–1905.
5. Monro, S., K. L. Colón, H. Yin, J. Roque, P. Konda, S. Gujar, R. P. Thummel, L. Lilge, C. G. Cameron and S. A. McFarland (2019) Transition metal complexes and photodynamic therapy from a tumor-centered approach: Challenges, opportunities, and highlights from the development of TLD1433. *Chem. Rev.* **119**, 797–828.
6. Mari, C., V. Pierroz, S. Ferrari and G. Gasser (2015) Combination of Ru(II) complexes and light: New frontiers in cancer therapy. *Chem. Sci.* **6**, 2660–2686.
7. Reeßing, F. and W. Szymanski (2017) Beyond photodynamic therapy: Light-activated cancer chemotherapy. *Curr. Med. Chem.* **24**, 4905–4950.
8. Mari, C., V. Pierroz, R. Rubbiani, M. Patra, J. Hess, B. Spingler, L. Oehninger, J. Schur, I. Ott, L. Salassa, S. Ferrari and G. Gasser (2014) DNA intercalating RuII polypyridyl complexes as effective photosensitizers in photodynamic therapy. *Chem. Eur. J.* **20**, 14421–14436.
9. Zayat, L., C. Calero, P. Alborés, L. Baraldo and R. Etchenique (2003) A new strategy for neurochemical Photodelivery: Metal−ligand heterolytic cleavage. *J. Am. Chem. Soc.* **125**, 882–883.
10. del Mármol, J., O. Filevich and R. Etchenique (2010) A ruthenium−rhodamine complex as an activatable fluorescent probe. *Anal. Chem.* **82**, 6259–6264.

11. Bonnet, S. (2018) Why develop photoactivated chemotherapy? *Dalton Trans.* **47**, 10330–10343.
12. Vaupel, P. and A. Mayer (2007) Hypoxia in cancer: Significance and impact on clinical outcome. *Cancer Metastasis Rev.* **26**, 225–239.
13. Cuello-Garibo, J.-A., M. S. Meijer and S. Bonnet (2017) To cage or to be caged? The cytotoxic species in ruthenium-based photoactivated chemotherapy is not always the metal. *Chem. Commun.* **53**, 6768–6771.
14. Li, A., R. Yadav, J. K. White, M. K. Herroon, B. P. Callahan, I. Podgorski, C. Turro, E. E. Scott and J. J. Kodanko (2017) Illuminating cytochrome P450 binding: Ru(II)-caged inhibitors of CYP17A1. *Chem. Commun.* **53**, 3673–3676.
15. Albani, B. A., B. Peña, N. A. Leed, N. A. B. G. de Paula, C. Pavani, M. S. Baptista, K. R. Dunbar and C. Turro (2014) Marked improvement in photoinduced cell death by a new tris-heteroleptic complex with dual action: Singlet oxygen sensitization and ligand dissociation. *J. Am. Chem. Soc.* **136**, 17095–17101.
16. Garner, R. N., J. C. Gallucci, K. R. Dunbar and C. Turro (2011) [Ru(bpy)2(5-cyanouracil)2]2+ as a potential light-activated dual-action therapeutic agent. *Inorg. Chem.* **50**, 9213–9215.
17. Lameijer, L. N., D. Ernst, S. L. Hopkins, M. S. Meijer, S. H. C. Askes, S. E. Le Dévédec and S. Bonnet (2017) A red-light-activated ruthenium-caged NAMPT inhibitor remains phototoxic in hypoxic cancer cells. *Angew. Chem. Int. Ed.* **56**, 11549–11553.
18. Kraus, D., J. Reckenbeil, N. Veit, S. Kuerpig, M. Meisenheimer, I. Beier, H. Stark, J. Winter and R. Probstmeier (2018) Targeting glucose transport and the NAD pathway in tumor cells with STF-31: A re-evaluation. *Cell. Oncol.* **41**, 485–494.
19. Chan, D. A., P. D. Sutphin, P. Nguyen, S. Turcotte, E. W. Lai, A. Banh, G. E. Reynolds, J.-T. Chi, J. Wu, D. E. Solow-Cordero, M. Bonnet, J. U. Flanagan, D. M. Bouley, E. E. Graves, W. A. Denny, M. P. Hay and A. J. Giaccia (2011) Targeting GLUT1 and the Warburg effect in renal cell carcinoma by chemical synthetic lethality. *Sci. Transl. Med.* **3**, 94ra70.
20. Kausch, I., M. Sommerauer, F. Montorsi, A. Stenzl, D. Jacqmin, P. Jichlinski, D. Jocham, A. Ziegler and R. Vonthein (2010) Photodynamic diagnosis in non-muscle-invasive bladder cancer: A systematic review and cumulative analysis of prospective studies. *Eur. Urol.* **57**, 595–606.
21. Matoba, Y., K. Banno, I. Kisu and D. Aoki (2018) Clinical application of photodynamic diagnosis and photodynamic therapy for gynecologic malignant diseases: A review. *Photodiagn. Photodyn. Ther.* **24**, 52–57.
22. Fukuhara, H., S. Yamamoto, T. Karashima and K. Inoue (2021) Photodynamic diagnosis and therapy for urothelial carcinoma and prostate cancer: New imaging technology and therapy. *Int. J. Clin. Oncol.* **26**, 18–25.
23. Malik, Z. (2020) Fundamentals of 5-aminolevulinic acid photodynamic therapy and diagnosis: An overview. *Transl. Biophotonics* **2**, e201900022.
24. Kostron, H. (2014) Photodynamic diagnosis and therapy for brain malignancies from the bench to clinical application. In *Photodynamic Therapy: From Theory to Application* (Edited by M. H. Abdel-Kader), pp. 165–184. Springer, Berlin Heidelberg: Berlin, Heidelberg.
25. Mallidi, S., B. Q. Spring and T. Hasan (2015) Optical imaging, photodynamic therapy and optically triggered combination treatments. *Cancer J.* **21**, 194–205.
26. Siewert, B., M. Langerman, Y. Hontani, J. T. M. Kennis, V. H. S. van Rixel, B. Limburg, M. A. Siegler, V. Talens Saez, R. E. Kieltyka and S. Bonnet (2017) Turning on the red phosphorescence of a [Ru(tpy)(bpy)(Cl)]Cl complex by amide substitution: Self-aggregation, toxicity, and cellular localization of an emissive ruthenium-based amphiphile. *Chem. Commun.* **53**, 11126–11129.
27. Rotman, B. and B. W. Papermaster (1966) Membrane properties of living mammalian cells as studied by enzymatic hydrolysis of fluorogenic esters. *Proc. Natl. Acad. Sci. U. S. A.* **55**, 134–141.
28. Lavis, L. D., T.-Y. Chao and R. T. Raines (2006) Fluorogenic label for biomolecular imaging. *ACS Chem. Biol.* **1**, 252–260.
29. Molenaar, C., J.-M. Teuben, R. J. Heetebrij, H. J. Tanke and J. Reedijk (2000) New insights in the cellular processing of platinum antitumor compounds, using fluorophore-labeled platinum complexes and digital fluorescence microscopy. *J. Biol. Inorg. Chem.* **5**, 655–665.
30. Liederer, B. M. and R. T. Borchardt (2006) Enzymes involved in the bioconversion of ester-based prodrugs. *J. Pharm. Sci.* **95**, 1177–1195.
31. Dong, H., L. Pang, H. Cong, Y. Shen and B. Yu (2019) Application and design of esterase-responsive nanoparticles for cancer therapy. *Drug Deliv.* **26**, 416–432.
32. Afrimzon, E., A. Deutsch, Y. Shafran, N. Zurgil, J. Sandbank, I. Pappo and M. Deutsch (2008) Intracellular esterase activity in living cells may distinguish between metastatic and tumor-free lymph nodes. *Clin. Exp. Metastasis* **25**, 213–224.
33. Breslow, R. (1991) Hydrophobic effects on simple organic reactions in water. *Acc. Chem. Res.* **24**, 159–164.
34. Vonlanthen, M., A. Cevallos-Vallejo, E. Aguilar-Ortíz, A. Ruiu, P. Porcu and E. Rivera (2016) Synthesis, characterization and photophysical studies of novel pyrene labeled ruthenium (II) trisbipyridine complex cored dendrimers. *Polymer* **99**, 13–20.
35. Weinstein, J. N. and L. D. Leserman (1984) Liposomes as drug carriers in cancer chemotherapy. *Pharmacol. Ther.* **24**, 207–233.
36. Adler-moore, J. P. and R. T. Proffitt (1993) Development, characterization, efficacy and mode of action of Ambisome, a Unilamellar liposomal formulation of amphotericin B. *J. Liposome Res.* **3**, 429–450.
37. Bonnet, S., B. Limburg, J. D. Meeldijk, R. J. M. Klein Gebbink and J. A. Killian (2011) Ruthenium-decorated lipid vesicles: Light-induced release of $[Ru(terpy)(bpy)(OH_2)]^{2+}$ and thermal Back coordination. *J. Am. Chem. Soc.* **133**, 252–261.
38. Orellana, E. A. and A. L. Kasinski (2016) Sulforhodamine B (SRB) assay in cell culture to investigate cell proliferation. *Bio-Protocol* **6**, e1984.
39. Zhou, X.-Q., A. Busemann, M. S. Meijer, M. A. Siegler and S. Bonnet (2019) The two isomers of a cyclometallated palladium sensitizer show different photodynamic properties in cancer cells. *Chem. Commun.* **55**, 4695–4698.
40. DeRosa, M. C. and R. J. Crutchley (2002) Photosensitized singlet oxygen and its applications. *Coord. Chem. Rev.* **233-234**, 351–371.
41. Garcìa-Fresnadillo, D., Y. Georgiadou, G. Orellana, A. M. Braun and E. Oliveros (1996) Singlet-oxygen (1Δg) production by ruthenium(II) complexes containing polyazaheterocyclic ligands in methanol and in water. *Helv. Chim. Acta* **79**, 1222–1238.